EPR Polarization Studies on Mn Catalase from *Lactobacillus plantarum*†

Alexandre E. Meier, Mei M. Whittaker, and James W. Whittaker*

Department of Chemistry, Carnegie Mellon University, 4400 Fifth Avenue, Pittsburgh, Pennsylvania 15213

Received September 7, 1995; Revised Manuscript Received November 14, 1995⊗

ABSTRACT: The binuclear manganese active site of Mn catalase catalyzes redox disproportionation of hydrogen peroxide, forming dioxygen and water. We report here multifrequency EPR and microwave polarization studies of the catalytically active homovalent Mn^{2+} complex of *Lactobacillus plantarum* Mn catalase, resolving spectra from each of the thermally accessible multiplet states of the coupled complex by multivariate methods. The experimental spectra have been simulated using computational approaches for the binuclear cluster to predict both *intensity* and *polarization* for arbitrary values of the ground state parameters. These two spectroscopic properties define the nature of the ground state wavefunctions and so serve as a sensitive and quantitative measure of the inter-ion interactions in the reduced complex. Interpretation of the spectra in terms of a pair Hamiltonian that includes Heisenberg exchange, dipolar, single site zero field splitting, and Zeeman perturbations leads to the most complete ground state description of the active site metal centers. The results of this spectroscopic analysis support a picture of two high spin ions weakly coupled by exchange interactions ($J = 40$ cm^{-1}) with relatively small dipole−dipole coupling and single site zero field splittings for the ligand-free reduced enzyme. The coupling between fluoride binding and protonation of the complex has been demonstrated by proton uptake studies. The binding of two fluoride ions in the active site dramatically changes the pair spectra, reflecting a substantially reduced *J*-coupling ($J = 10.5$ cm^{-1}) that must be a consequence of perturbation of the bridging ligands. Anion binding to the binuclear Mn complex appears to result in poisoning of the active site by protons, possibly associated with insertion of fluoride into bridging positions of the dimanganese core.

Catalases are ubiquitous metalloenzymes that catalyze the redox disproportionation of hydrogen peroxide into water and oxygen:

$$2H_2O_2 \rightarrow 2H_2O + O_2 \quad (1)$$

thus complementing superoxide dismutases in biological defenses against toxic oxygen metabolites (Beyer & Fridovich, 1988). This reaction is spontaneous and peroxide is unstable under physiological conditions but significant kinetic activation barriers exist for the direct, uncatalyzed, reaction. Catalases function by uncoupling the two half-reactions of peroxide reduction (eq 2) and oxidation (eq 3), storing electrons and protons between the two redox steps. While the majority of catalases contain a heme cofactor, nonheme binuclear manganese catalases have been found to perform this essential function in microorganisms inhabiting iron-deficient environments (Felton et al., 1953; Whittenbury, 1964). The best studied of these alternative catalases have been isolated from the bacteria *Thermus thermophilus* (Khangulov et al., 1990a−c) and *Lactobacillus plantarum* (Kono & Fridovich, 1983; Penner-Hahn, 1992).

Although the heme enzyme contains a mononuclear metal center and the nonheme enzyme a binuclear metal complex, heme and nonheme catalytic active sites both serve as two-electron redox units, matching the requirements of each of the individual half reactions (eqs 2 and 3, below). In the heme enzyme, iron and tetrapyrrole both participate in the redox chemistry, forming a porphyrin π cation radical on oxidation (Schonbaum & Chance, 1976). In the nonheme enzyme, both Mn ions undergo oxidation and reduction in the catalytic cycle, shuttling between homovalent (Mn^{3+} Mn^{3+}) and (Mn^{2+} Mn^{2+}) forms (Khangulov et al., 1990a−c; Waldo & Penner-Hahn, 1995). The chemistry of Mn catalase is of special interest as a model for the reactions that occur in photosynthetic oxygen evolution (eq 4), which can be envisioned as involving elementary steps corresponding to the two half-reactions of the catalase disproportionation cycle:

$$2H_2O \leftrightarrow H_2O_2 + 2\,e^- + 2\,H^+ \quad (2)$$

$$H_2O_2 \leftrightarrow O_2 + 2\,e^- + 2\,H^+ \quad (3)$$

$$2H_2O \rightarrow O_2 + 4\,e^- + 4\,H^+ \quad (4)$$

This chemical analogy may go deeper, since a tetranuclear Mn cluster has been identified as the active site for water oxidation in the photosynthetic apparatus of green plants (Chenaie & Martin, 1970; Radmer & Chenaie, 1977; Brodsky & Frasch, 1985).

Biology has evolved cluster complexes for a variety of functions including electron transfer (Spiro, 1982; Fee et al., 1995), dioxygen binding (Stenkamp, 1994; Magnus et al., 1994), and catalysis (Rosenweig et al., 1993). The electronic coupling between the interacting metal ions in the complex, determined by structure (Reed & Orosz, 1993), in turn defines the characteristic redox reactivity of a cluster. Strong covalency, reflected in large exchange splittings, is associated with *molecular* reactivity for the coupled complex, while weaker interactions result in independent, uncoupled reactivity typical of the isolated ions. The strongly coupled, bis-

† Support for this project from the National Institutes of Health (GM 42680 to J.W.W.) is gratefully acknowledged.

* Corresponding author. Telephone: 412-268-5670. Fax 412-268-6945. E-mail: jim@insight.chem.cmu.edu.

⊗ Abstract published in *Advance ACS Abstracts,* December 15, 1995.

0006-2960/96/0435-348$12.00/0

(μ-sulfide)-bridged binuclear iron core in plant ferredoxins, an example of a strongly coupled complex [$J = 366$ cm^{-1}, antiferromagnetic exchange (Palmer et al., 1971)], exhibits single-electron redox chemistry with a large shift in potential between successive redox steps. In contrast, weakly coupled complexes undergo two-electron redox processes with virtually no splitting in potential between the two sites. While exchange interactions are small compared to chemical binding energies and so have no *direct* influence on chemistry, these splittings *do* reflect (on a small scale) the charge transfer and covalency terms that determine activation barriers for electron transfer and the energetic stabilities of different structures (Noodleman & Case, 1992; Mouresecu et al., 1994). These electronic interactions are generally oxidation state-dependent, with dramatic differences evident between oxidized and reduced complexes. However, typical exchange splittings for oxygen- and carboxylate-bridged binuclear Mn complexes are in the range 1−50 cm^{-1} for both Mn^{2+} and Mn^{3+} binuclear complexes (Ménage et al., 1988; Vincent & Christou, 1989; Tofflund et al., 1990).

In order to more fully understand the electronic factors important for O_2 and peroxide interactions and redox properties of the binuclear Mn active site of Mn catalase, we have applied a combination of multifrequency EPR[1] and microwave polarization studies to experimentally probe the ground state of the reduced binuclear complex. The individual spectral components arising from discrete S_T multiplets of the coupled complex, resolved using singular value decomposition techniques to reduce the data matrices, contain information on the electronic wavefunctions that can be interpreted by complete spectroscopic simulation based on a Hamiltonian for the binuclear complex that includes Heisenberg exchange, magnetic dipolar, spin orbit coupling, and Zeeman terms, providing quantitative estimates of the wavefunctions and energy splittings. Exact solution of this 36-dimensional pair Hamiltonian and calculation of intensity and polarization for magnetic dipole transitions among the sublevels yields theoretical solution spectra for comparison with the experimental data. This approach to complete simulation of transition fields, intensities, and polarizations provides the best estimate of ground state parameters leading to insight into the structural determinants of active site reactivity.

EXPERIMENTAL PROCEDURES

Biological Preparations. L. plantarum (ATCC 14431) was grown in APT medium under continuous aeration for 12 h and the Mn catalase isolated according to published procedures (Kono & Fridovich, 1983; Beyer & Fridovich, 1985). Metal ion analyses obtained for samples of *L. plantarum* Mn catalase are consistent with nearly full Mn content (>11 Mn) for the purified protein if a hexameric structure is assumed, as found for the *T. thermophilus* enzyme (Khangulov et al., 1995), rather than the unusual pentameric subunit composition recently suggested (Beyer & Fridovich, 1985). The analysis is consistent with as much as 15% half-occupied sites in some protein samples. Enzyme preparations consistently exhibit specific activity >7200 units/mg of protein (1 unit of enzyme decomposes 1 μmol of H_2O_2/min). Reduced Mn catalase was prepared for spectroscopic studies by anaerobic hydroxylamine titration under argon followed by desalting over a P-30 column equilibrated with deaerated buffer. The colorless reduced protein eluting from the column was detected by illuminating a short section quartz capillary inserted in the eluent path and observing the quenching of luminescence from a fluorescent thin layer chromatography plate. Protein collected in argon-purged sample vials was transferred anaerobically into EPR sample tubes flushed with argon and frozen slowly in liquid nitrogen.

Spectroscopic Measurements. EPR spectra were recorded on a Bruker ER300 EPR spectrometer with an X-Band microwave bridge and Bruker ER4116 DM bimodal cavity resonating with microwave magnetic field parallel or perpendicular to the direction of the applied magnetic field in longitudinal or transverse mode. Temperature control was provided by an Oxford Instruments ESR Model 900 helium flow cryostat (4−100 K temperature range) equipped with backflow control for temperature stabilization and using an Fe(Au)-chromel thermocouple sensor positioned below the sample for temperature measurement. Temperature readings were calibrated by recording the spectrum of a capillary sample of manganous phosphate over the effective temperature range and fitting the temperature-dependent EPR signal intensity to a Curie Law curve. Nonsaturating microwave power levels were used throughout these experiments to ensure the validity of the intensity information. Q-Band spectra were recorded at the National Biomedical ESR Center in Milwaukee. Metal ion analyses were performed on a Varian Instruments Model SpectrAA 20B atomic absorption spectrometer equipped with a GTA-96 graphite furnace for high sensitivity analytical determinations. Optical absorption measurements were performed on a Varian Cary 5 UV−vis−NIR absorption spectrometer.

Potentiometric Titration. Fluoride binding by reduced Mn catalase was detected potentiometrically using a Microelectrodes Inc. fluoride ion-sensitive electrode. $Mn^{2+/2+}$ catalase, prepared anaerobically and desalted into 50 mM sodium acetate buffer, pH 5.5, or 50 mM potassium phosphate buffer, pH 7.0, as described above, was progressively titrated with KF and the fluoride potential, reflecting the concentration of free fluoride ion, measured for comparision with a calibration curve prepared under identical conditions.

Proton Uptake Measurements. Proton uptake coupled to anion binding by reduced Mn catalase was determined quantitatively on enzyme initially equilibrated with 50 mM sodium acetate buffer (pH 5.5). Samples were prepared by desalting the enzyme in carbonate-free, argon-purged solution buffered only by the protein (82 μM active sites) and adding 1 equiv of pH indicator dye (bromocresol purple, 80 μM final concentration) to 1 mL final volume. Absorption changes resulting from the perturbed protonation state of the indicator were calibrated by addition of standard NaOH solution (aliquots yielding 41 μM base in the sample). Fluoride was added to saturation [two steps of 2 μmol each, $>10K_{D,2}(F^-)$] followed by recalibration (Whittaker & Whittaker, 1993; Whittaker, 1994).

EPR Data Analysis. EPR spectral data obtained over a range of temperatures were compiled into data matrices and reduced by singular value decomposition (SVD) to a set of linearly independent components (Press et al., 1992; Henry & Hofrichter, 1992). SVD leads to the best solution for orthogonal basis eigenvectors of the data in a least-squares

[1] Abbreviations: EPR, electron paramagnetic resonance; SVD, singular value decomposition.

sense. Based on the magnitudes of the singular values, the rank of the matrix of spectra was reduced to three components, which were subsequently transformed into physical basis vectors by a unitary multiplication based on the temperature dependence of a *J*-coupling model. The quality of fit for a given value of *J* was determined by summing the squares of the residuals in the difference matrix. The details of this procedure are outlined below.

Following baseline subtraction, the experimental spectra obtained over a range of temperatures were compiled into a rectangular ($n \times m$) data matrix **D** with apparent rank *n* equal to the number of temperatures at which spectra were recorded. Standard singular value decomposition routines (e.g., in Mathematica) allow linear resolution of the data matrix into orthogonal eigenvector matrices **U** and **V** representing eigenvector decomposition of $\mathbf{DD}^{\mathrm{T}}$ and $\mathbf{D}^{\mathrm{T}}\mathbf{D}$ product matrices, respectively:

$$\mathbf{D} = \mathbf{U}^{\mathrm{T}}\lambda\mathbf{V} \tag{5}$$

In this matrix equation, λ is a diagonal matrix of eigenvalues, the singular values whose magnitudes reflect the relative importance of each of the basis vectors. In the present case, resolution of **D** yields spectral basis vectors in **U** and the corresponding conditional vectors (the temperature dependence of the basis spectra) in **V**. This decomposition provides the best separation of the data (in a least-squares sense) into linearly independent components. By retaining only the largest eigenvectors of **U** based on their singular values, the quality of the spectra is dramatically improved, effectively averaging over all spectra simultaneously in the projection of the entire data into the rank-reduced subspace **D′**:

$$\mathbf{D}' = (\mathbf{U}^{\mathrm{T}})'\lambda\mathbf{V}' \tag{6}$$

However, the basis vectors obtained by SVD analysis are in general not unique and represent linear combinations of physical spectra associated with the largest singular values and noise (Henry & Hofrichter, 1992). These combinations can be unmixed to recover the true physical components by applying a basis transformation defined by a physical model. In the present case, thermal population over a spin ladder can be used to construct a model temperature dependence matrix, **T**, whose rows give the normalized intensity expected for each temperature point at which data was recorded. The intensities are computed from the population difference between neighboring levels within a *J*-multiplet thermalized with a Boltzmann statistical distribution:

$$I = I_{\mathrm{o}}(\mathrm{e}^{-E_i/kT} - \mathrm{e}^{-E_j/kT})/Q \tag{7}$$

where the partition function is

$$Q = \sum_s (2S + 1)\, \mathrm{e}^{-E(S)/kT} \tag{8}$$

and the multiplet energies are

$$E(S_{\mathrm{T}}) = J/2[S_{\mathrm{T}}(S_{\mathrm{T}} + 1) - S_1(S_1 + 1) - S_2(S_2 + 1)] \tag{9}$$

The unitary transformation (rotation of basis) that converts **V** into **T** is then given by

$$\mathbf{R}^{-1} = \mathbf{T}(\mathbf{V}^{\mathrm{T}}\mathbf{V})^{-1} \tag{10}$$

where **T** is the test matrix of temperature conditional vectors computed from the physical model, and $(\mathbf{V}^{\mathrm{T}}\mathbf{V})^{-1}$ is the pseudoinverse of the rectangular matrix **V**. Since the numerical stability of the pseudoinverse depends on how far the matrix deviates from square form, the number of field points is in general reduced from the full number available. Equation 10 also provides the transformation matrix **R** required to convert the basis of the SVD orthogonal eigenvector matrix **U′** into a physical basis, by projecting onto the conditional vectors in **T**.

Right-multiplication by the unitary matrix **R** transforms the rank-reduced matrix of spectra (**U′**) into the physical basis components of the data, while left-multiplication of the row matrix of the reduced conditional vectors **V′** by the corresponding inverse transformation $\mathbf{R}^{-1}$ yields conditional eigenvectors that are consistent with the physical model:

$$\mathbf{D}' = (\mathbf{U}^{\mathrm{T}})'\lambda\mathbf{R}\mathbf{R}^{-1}\mathbf{V}' \tag{11}$$

The appropriateness of the model is measured by the magnitude of the sum of squares of residuals that are the elements of the error matrix **E**, the difference between the prediction matrix **T** and the transformed conditional matrix **T′**:

$$\mathbf{T}' = \mathbf{R}^{-1}\mathbf{V}' \tag{12}$$

$$\mathbf{E} = \mathbf{T}' - \mathbf{T} \tag{13}$$

$$\mathrm{Err} = \sum_i \sum_j (E_{ij})^2 = \sum_i \sum_j (\mathbf{T}'_{ij} - \mathbf{T}_{ij})^2 \tag{14}$$

Optimization is achieved by minimizing the magnitude of this error, providing the best estimate of the magnitude of the exchange splitting, *J*, the variable parameter used in the fitting procedure, by fitting the entire matrix simultaneously. These manipulations are efficiently performed within symbolic mathematical program libraries such as Mathematica or Matlab.

Simulations. Program nu_spin, a numerical spectral simulation program, was developed for calculation of pair spectra for coupled binuclear high-spin d^5 metal ions and solves for resonance fields under the combined exchange, dipolar, spin orbit, and Zeeman perturbations, computing the intensities and polarizations of the resulting spectra. Theoretical results corresponding to rotationally averaged solution spectra are built by summing over an angular grid using a modified Simpson's Rule integration routine (Press et al., 1992). nu_spin was compiled under the 64-bit Irix 6.0 operating system and runs on a Silicon Graphics Power Indigo^2 Unix workstation.

SPECTROSCOPIC RESULTS AND DISCUSSION

Spectroscopic Consequences of Anion Binding. The broad, overlapping spectra of the reduced binuclear Mn cluster of *L. plantarum* Mn catalase (Figure 1, top) and its fluoride adduct (Figure 1, bottom) are complex, covering a magnetic field range of greater than 1.5 Tesla with significant absorption extending to the zero field limit. Trains of nuclear hyperfine features of high multiplicity are resolved on many of the signals (e.g., Figure 4) clearly identifying them as arising from the coupled complex. The complex is fully reduced on the basis of optical spectroscopy, ensuring that all of the observed resonances originate from Mn^{2+}. The

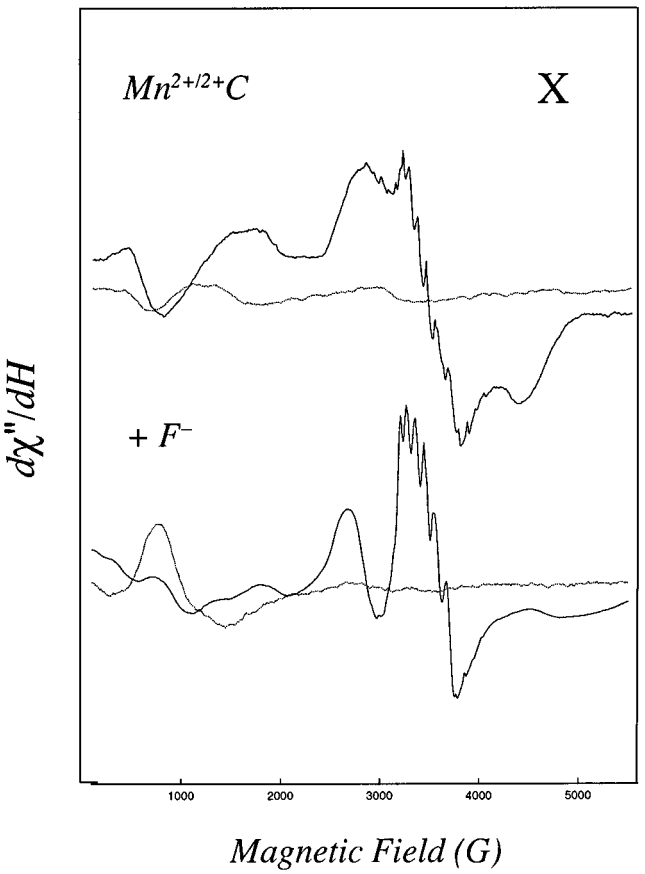

FIGURE 1: X-band EPR spectra for reduced Mn catalase complexes. (Top) $Mn^{2+/2+}$ catalase in 50 mM $KHPO_4$ buffer, pH 7. (Bottom) Fluoride complex (100 mM KF). Instrumental parameters: frequency (9.65 GHz, perpendicular; 9.36 GHz, parallel), microwave power (1 mW), modulation amplitude (10 G), modulation frequency (100 kHz), temperature [20 K (top), 5 K (bottom)]. Solid line, perpendicular polarization; dotted line, parallel polarization at same gain.

spectra of the two forms (Figure 1) resemble each other but are clearly distinct, reflecting a significant perturbation by fluoride in the anion complex. The spectra are most clearly distinguished by their markedly different temperature dependences (see below). Spectra from the unliganded protein virtually vanish at the lowest temperatures, while significant intensity remains in the EPR spectra of the fluoride complex even at 4 K.

Fluoride interactions have been observed previously for both the *T. thermophilus* and *L. plantarum* enzymes (Khangulov et al., 1990c, 1995; Waldo & Penner-Hahn, 1995), with similar effects found for a range of other ions (azide, chloride, phosphate, borate) for the former protein. For *L. plantarum* Mn catalase, we find that fluoride is an effective inhibitor, but no significant effect is detected with phosphate or chloride at neutral pH. In order to obtain more information about anion interactions in the Mn catalase active site, we have measured the dissociation constant for fluoride from the oxidized Mn^{3+} form of the enzyme in a spectrophotometric titration and find a pH-dependent affinity for the active site complex: $K_D = 0.5$ mM (pH 5.5); $K_D = 14$ mM (pH 7). While the reduced Mn^{2+} enzyme lacks optical absorption features that can be used to detect fluoride binding, the unbound fraction of fluoride in the sample can be measured potentiometrically to monitor the progress of the titration (Figure 2, top, insert). Under stoichiometric titration conditions (enzyme concentration in excess over the estimated K_D),

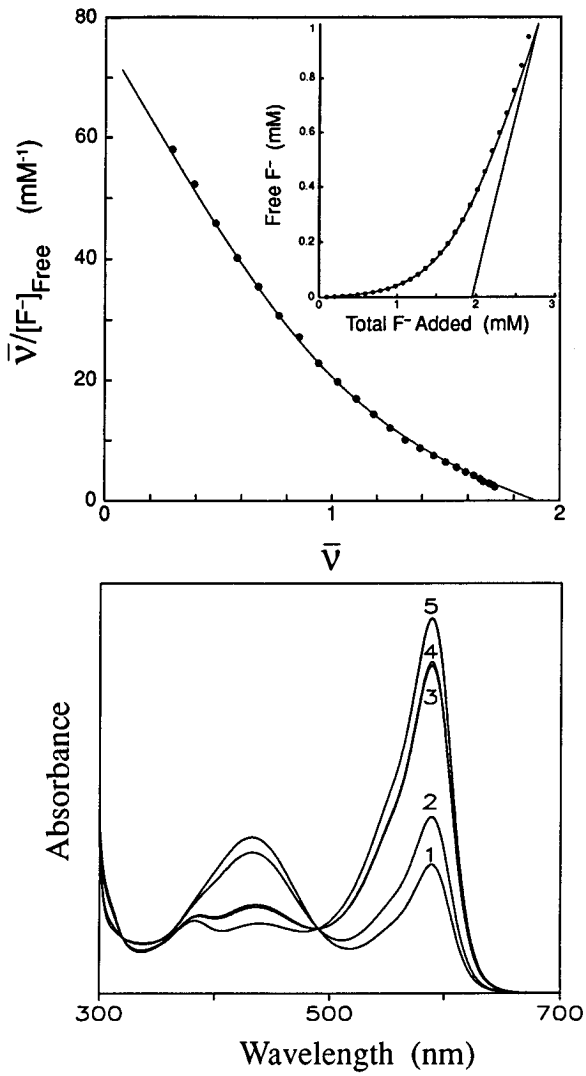

FIGURE 2: (Top) Potentiometric fluoride titration of reduced Mn catalase. (Inset) Free fluoride concentration measured as a function of total fluoride added to Mn catalase in 50 mM sodium acetate buffer, pH 5.5. The data (●) are fit by theory for independent two-site binding with $K_{D,1} = 12$ μM and $K_{D,2} = 140$ μM obtained by Scatchard analysis of the data (lower panel). The hyperbolic Scatchard plot of $\nu/[F^-]_{Free}$ versus the bound fraction ν provides estimates of the binding parameters. The parametric equations solved for these parameters were plotted as the theoretical curve (solid line). (Bottom) Proton coupled anion binding by reduced Mn catalase. Mn catalase (82 μM active sites) prepared in argon-purged, carbonate-free solution buffered only by 80 μM bromocresol purple pH indicator dye was adjusted by addition of 15 μL of 20.5 mM NaOH (spectrum 1) and the colorimetric response of the indicator calibrated by further addition of 41 pmol of NaOH (spectrum 2) before addition of two saturating aliquots of KF (to 2 and 4 mM final concentrations fluoride, spectra 3 and 4) and a second calibration by addition of 41 pmol of NaOH (spectrum 5).

the unbound ion concentration curve exhibits a break at the point of saturation of protein binding sites. For a sample containing 0.95 mM active sites, the break point determined by extrapolation from the limiting high-concentration slope occurs at 2 equiv of fluoride bound (Figure 2, top, insert), providing direct evidence for binding of two fluoride ions per active site at saturation. A Scatchard analysis of the binding data (Dahlquist, 1978) (Figure 2, top) permits resolution of these binding steps and provides quantitative estimates of binding affinities. The higher affinity complex ($K_D = 12$ μM) is nearly an order of magnitude more tightly bound than the lower affinity complex ($K_D = 140$ μM). The

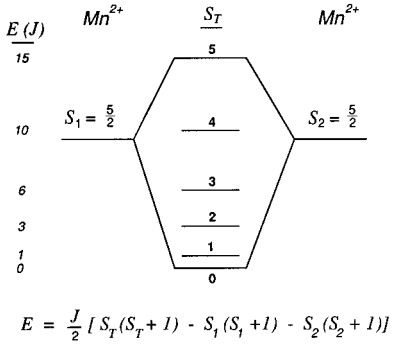

FIGURE 3: Heisenberg exchange ladder for coupled binuclear high spin Mn^{2+} complex.

2:1 stoichiometry of the saturated complex indicates that two distinct sites must be available for binding exogenous ligands. At pH 7.0, the tighter complex has $K_D = 260\ \mu M$.

The pH dependence of the fluoride affinities suggests a coupling between anion binding and proton equilibria in the active site. This possibility was explored by measuring proton uptake coupled to fluoride binding in reduced Mn catalase complexes (Figure 2, bottom). At low pH, it is possible to titrate the complexes with fluoride to a saturation endpoint and detect deprotonation of bromocresol purple reflecting proton uptake by the enzyme in the anion adduct. The number of protons bound in the fluoride complex can be determined by calibrating the signal from the indicator dye using aliquots of standard base (Figure 2, bottom, spectra 2 and 5). The deprotonation of the indicator is clearly not a result of hydrolysis by the fluoride ion, since no further change was detected after a second addition of the same amount of fluoride solution (Figure 2, bottom, spectrum 4). Analysis of these spectra indicate that 1.6−1.7 protons are bound in each active site as a result of fluoride interactions.

EPR spectra of the fluoride-saturated $Mn^{2+/2+}$ catalase complex recorded at pH 5.5 are essentially identical to those recorded at pH 7 except for an increased resolution of Mn hyperfine structure in several spectral features. No additional splittings that might be attributable to ^{19}F nuclear hyperfine coupling have been detected in these spectra, consistent with the weak covalency expected for the divalent manganese ion. Under turnover conditions in the presence of hydrogen peroxide, fluoride traps the enzyme in the reduced state. This anion inhibition is reversible, and full activity is recovered on removal of the fluoride by dialysis. Identical complexes are formed by hydroxylamine reduction followed by addition of NaF or by F^-/peroxide treatment (turnover inactivation). There is no evidence for O_2 binding in the reduced protein, the same spectrum being observed for enzyme prepared anaerobically or exposed to air.

Temperature-Dependent EPR Spectra. Changes in the EPR spectra resulting from systematically varying the sample temperature reflect thermal population over ground state sublevels of the coupled binuclear complex split by exchange interactions (Figure 3). If the lowest level is paramagnetic, a pure spectrum can always be obtained at sufficiently low temperature, where only the lowest sublevels are thermally populated. However, when the lowest sublevel is diamagnetic, as is the case for the antiferromagnetically coupled homovalent dimer illustrated in Figure 3, the spectra are always a mixture of contributions from different multiplets of the spin ladder. These broad and overlapping spectra will not be resolved by simple temperature variation, but the linear

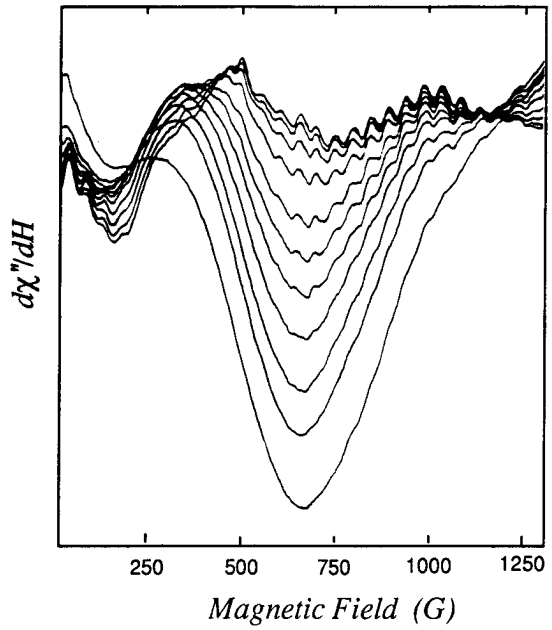

FIGURE 4: Temperature-dependent low field X-band EPR spectra for $Mn^{2+/2+}$ catalase. Instrumental parameters are as described in the legend to Figure 1 with temperatures 10, 15, 20, 25, 30, 35, 40, 50, 60, 70, and 80 K.

components can be deconvoluted by SVD methods (see below). Sorting the spectral components on the basis of temperature dependence yields discrete spectra from within each S_T multiplet. Because of the expanding ladder, with intervals proportional to S_T (Landé rule splittings) only the lowest multiplets contribute significantly to the experimental spectra over the temperature range of these experiments. These spectra arising from excited multiplets exhibit dramatically non-Curie behavior, strongly deviating from $1/T$ temperature dependence. However, each component has a unique and characteristic temperature dependence, determined by the Boltzmann thermal distribution over the spin ladder, allowing the resolution to be performed. Spectra arising within any S_T multiplet will exhibit the same temperature dependence allowing the spectra to be projected onto this restricted set of temperature profiles in sorting into linearly independent basis components. Small variations in the partition function associated with the increasing Zeeman splittings across the field swept spectrum, and exchange striction effects (Harris, 1972), are not resolved at this level. In the moderate exchange limit characteristic of binuclear Mn^{2+} complexes, the spin ladder (Figure 3) appears to effectively model the ground state splittings.

The temperature variation of the EPR spectra for the ligand-free enzyme is complex. From virtually no detectable signals at the lowest temperatures, low-field resonances grow in and subsequently decay (Figure 4) with changes in resolved nuclear hyperfine from ^{55}Mn over this temperature range reflecting the distinct character of the resonances observed at different temperatures. At the highest temperatures, the most intense features of the spectrum appear near the free electron g value ($g = 2$) (Figure 5). The results for the fluoride complex are similar, but more extreme variation is evident over a lower temperature range (Figure 6).

Polarization Studies. Polarization measurements can resolve complex spectra, labeling transitions with additional spectroscopic information beyond the resonance condition (Kliger et al., 1990). Distinct EPR selection rules apply for

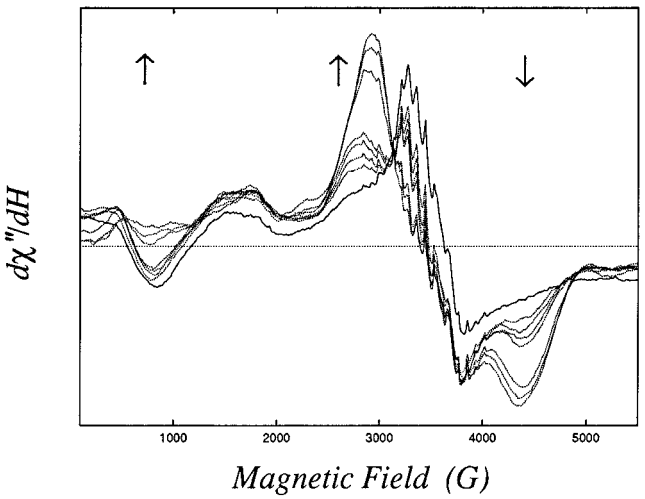

FIGURE 5: Temperature-dependent wide field X-band EPR spectra for $Mn^{2+/2+}$ catalase. Instrumental parameters are as described in the legend to Figure 1 with temperatures 10, 14, 16, 18, 20, 30, 40, and 50 K.

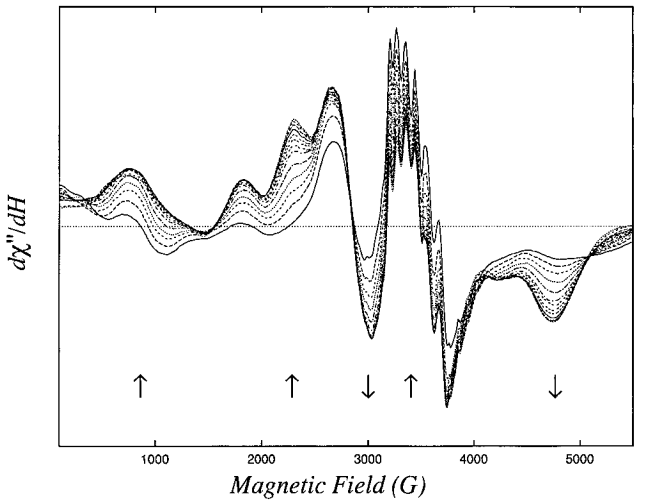

FIGURE 6: Temperature-dependent X-band EPR spectra for $Mn^{2+/2+}$ catalase-F^- in perpendicular polarization. Instrumental parameters are as described in the legend to Figure 1 with temperatures 4.1, 5, 6, 7, 8, 9, 10, 11, 12, 13, 14, 15, and 16 K.

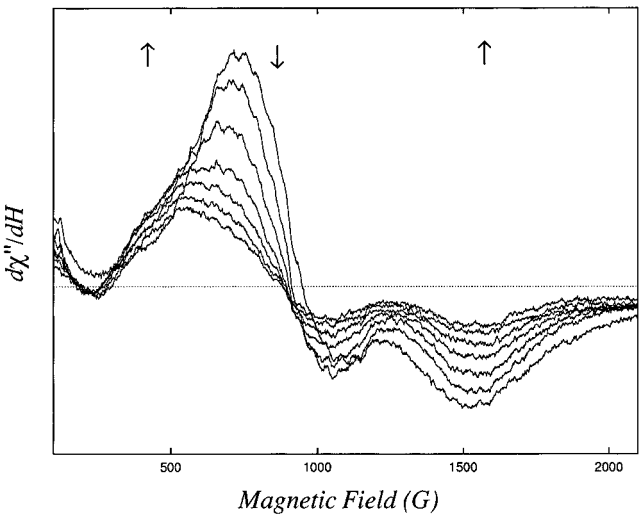

FIGURE 7: Temperature-dependent X-band EPR spectra for $Mn^{2+/2+}$ catalase-F^- in parallel polarization. Instrumental parameters are as described in the legend to Figure 1 with temperatures 10, 15, 20, 25, 30, 35, 40, 45, 50, 55, 60, 65, and 70 K.

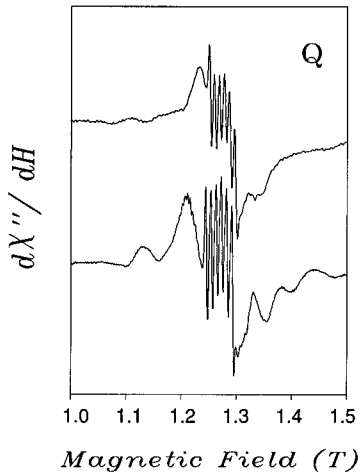

FIGURE 8: Q-Band EPR spectra for reduced Mn catalase complexes. (Top) $Mn^{2+/2+}$ catalase in 50 mM $KHPO_4$ buffer, pH 7. (Bottom) Fluoride complex (100 mM KF). Instrumental parameters: frequency (34.805 GHz), modulation amplitude (20 G), modulation frequency (100 kHz), temperature (30 K).

absorption of photons with polarization (microwave *magnetic* field vector) oriented parallel or perpendicular to the applied magnetic field (defining longitudinal and transverse Zeeman perturbations) further constraining the ground state wavefunctions. Figure 1 shows spectra for two forms of the enzyme described above in both polarizations (parallel and perpendicular). The largest polarization is observed for the low field resonance of the fluoride adduct which arises within the $S_T = 1$ multiplet (based on the temperature dependence) and acquires intensity from the relatively strong mixing of triplet sublevels by dipolar and zero field splitting perturbations (see below). As is expected for a simple Kramers system, the uncoupled mononuclear Mn signal near $g = 2$ (see below) is strongly suppressed in parallel polarization. The temperature dependence of these spectral features is shown in Figure 7. The origins of distinct polarization components requires consideration of the selection rules for each transition and is dealt with in more detail below, where simulation of polarization spectra is described.

Multifrequency EPR. Multifrequency EPR techniques can increase the information available from the resonance spectra of paramagnetic clusters, resolving frequency-dependent terms and simplifying the analysis. Multifrequency approaches are especially useful when resonances are associated with fictitious g values arising from intermediate mixing among Zeeman sublevels, as occurs in the present case where dipolar and spin orbit fine structure splittings occur in the cluster ground state. Distinct regions of the Zeeman spectrum are measured at Q-band and X-band. At Q-band (34.8 GHz, 1.2 cm^{-1}) the microwave quantum is four times the photon energy at X-band (9.4 GHz, 0.32 cm^{-1}), and as the photon energy is increased, the resonance fields are shifted accordingly, collapsing around the Zeeman-exchange limit of $g = 2$ in the high frequency experiments (Figure 8), where spectra form a symmetric pattern about the free electron g value decreasing in intensity away from the center. The largest shifts in these spectra are associated with the larger fine structure splittings that occur in states of lower multiplicity, as predicted from the irreducible tensor elements for intramultiplet splittings (Table 1, see below). Such transitions are intrinsically less intense than the

Table 1. Irreducible Tensor Components for Dipolar and Zero Field Splitting Elements

	H_{dip}	α^a	H_{zfs}	β^b
$\langle 1\|\|T^{(2)}\|\|1\rangle$	$37/(2\sqrt{15})$	37/10	$-16/\sqrt{15}$	−32/5
$\langle 2\|\|T^{(2)}\|\|0\rangle$	$-2\sqrt{(7/3)}$		$2\sqrt{(7/3)}$	
$\langle 2\|\|T^{(2)}\|\|1\rangle$	0		$2\sqrt{(6/5)}$	
$\langle 2\|\|T^{(2)}\|\|2\rangle$	$41/(2\sqrt{21})$	41/42	$-10/\sqrt{21}$	−20/21
$\langle 3\|\|T^{(2)}\|\|1\rangle$	$-18/\sqrt{35}$		$18/\sqrt{35}$	
$\langle 3\|\|T^{(2)}\|\|2\rangle$	0		$9/\sqrt{7}$	
$\langle 3\|\|T^{(2)}\|\|3\rangle$	$47/(3\sqrt{10})$	47/90	$-\sqrt{2}/(3\sqrt{5})$	−2/45
$\langle 4\|\|T^{(2)}\|\|2\rangle$	$-3\sqrt{(5/7)}$		$3\sqrt{(5/7)}$	
$\langle 4\|\|T^{(2)}\|\|3\rangle$	0		$5\sqrt{(2/3)}$	
$\langle 4\|\|T^{(2)}\|\|4\rangle$	$5\sqrt{(55/42)}$	5/14	$\sqrt{(110/21)}$	2/7
$\langle 5\|\|T^{(2)}\|\|3\rangle$	−5/3		5/3	
$\langle 5\|\|T^{(2)}\|\|4\rangle$	0		$\sqrt{15}$	
$\langle 5\|\|T^{(2)}\|\|5\rangle$	$(5\sqrt{65})/6$	5/18	$(2\sqrt{65})/3$	4/9
	$D_{0,0}^{(2)}(\phi,\theta,0) = 1/2(3\cos^2\theta - 1)$ $D_{\pm1,0}^{(2)}(\phi,\theta,0) = \mp(\sqrt{6}/2)\sin\theta\cos\theta\, e^{\mp i\phi}$ $D_{\pm2,0}^{(2)}(\phi,\theta,0) = (\sqrt{6}/4)\sin^2\theta\, e^{\mp 2i\phi}$		$D_{0,0}^{(2)}(\phi,\theta,0) = (1/2)(3\cos^2\theta - 1)$ $D_{\pm1,0}^{(2)}(\phi,\theta,0) = \mp(\sqrt{6}/2)\sin\theta\cos\theta\, e^{\mp i\phi}$	

^{a} $\alpha = -\sqrt{6}A_{00}^{S2S}\langle S||\mathbf{T}^{(2)}||S\rangle/(S(S+1))$. ^{b} $\beta = -2\sqrt{6}A_{00}^{S2S}\langle S||\mathbf{T}^{(2)}||S\rangle/(S(S+1))$.

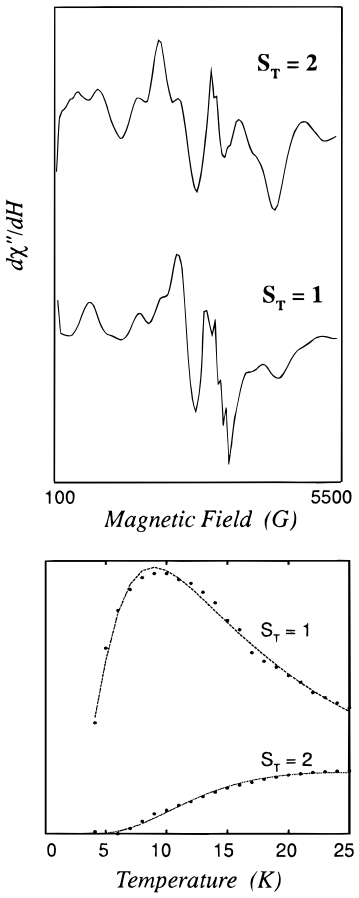

FIGURE 9: Resolved spectra for triplet and quintet states of the manganese exchange ladder for $Mn^{2+/2+}$ catalase-F^-. (Top) Eigenvectors extracted by singular value decomposition of the complete data matrix as described under Experimental Procedures. (Bottom) Experimental (···) and theoretical (---) temperature dependence vectors associated with the spectral components shown above. The theoretical lines correspond to Boltzmann functions for a Heisenberg exchange ladder with $J = 10.5$ cm^{-1}.

contributions from higher substates where the fine structure splittings are relatively small and the multiplicity is greater, implying more transitions contributing to a less anisotopic spectrum.

Deconvolution of Multiplet Spectra: SVD Linear Resolution of Component Spectra. Singular value decomposition is a powerful method of linear algebra useful for analyzing large sets of spectroscopic data. SVD analysis provides a least-squares fit on reduction of the data matrix and effectively averages over an entire data set, returning in the singular values information useful for significance testing. These methods have been extensively applied in analyzing diverse data: resolving orbital parameters of binary stars (Simon & Sturm, 1992), separating kinetic components in ultrafast spectra (Henry Hofrichter, 1992), mapping electrostatic potentials onto point charge distributions (Mouresca et al., 1994), and evaluating pH titration profiles (Shrager & Hendler, 1982). The SVD procedure applied to analysis of temperature-dependent EPR spectra is described in the Experimental Procedures.

Transformation to Physical Basis. As described above, the set of base spectra onto which the SVD analysis sorts the data is complete, spanning the data space, but is not unique and generally represents a linear combination of the physical spectral components. Physical spectra can be recovered by a unitary transformation that preserves the linear structure of the basis while constructing new combinations of initial vectors consistent with a conditional dependence (e.g., temperature variation) defined by a specific model. The appropriateness of a particular model is most readily gauged by evaluating the sum of squares of residuals after constructing an optimized conditional matrix in the reduced basis space (a least-squares method). For the unliganded enzyme, the best fit is obtained with $J = 40$ cm^{-1}, while a much smaller value ($J = 10.5$ cm^{-1}) is required to fit the data for the fluoride complex. Analysis of data for both polarizations for the fluoride complex gives the same optimized value for the exchange coupling (Figure 9). The resolved spectra for the triplet and quintet levels ($S_T = 1, 2$) closely resemble the corresponding spectra recently reported for the *T. thermophilus* Mn catalase phosphate complex (Khangulov et al., 1995).

Detection of Uncoupled Mn^{2+} Kramers Component. Application of SVD to the temperature-dependent X-band EPR spectra for the Mn catalase complexes led to the recognition of an eigenvector associated with a simple paramagnetic signal near $g = 2$ exhibiting Curie Law temperature dependence (Figure 10). The six-fold multiplicity of the hyperfine splitting of this signal and its polarization behavior allow the component to be identified as a minority mono-

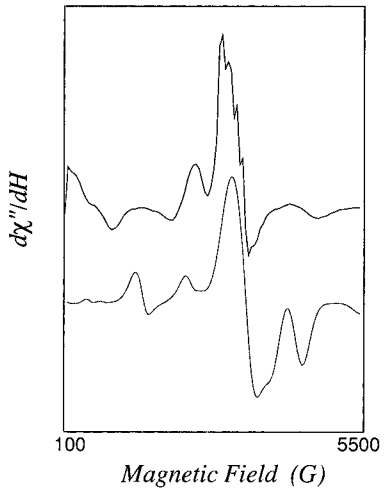

FIGURE 10: Resolved spectrum of the monomeric Mn^{2+} component in the $Mn^{2+/2+}$ catalase-F^- complex. (Above) Data eigenvector projected by SVD onto a Curie-law temperature dependence vector. (Below) Theoretical spectrum calculated for an $S = 5/2$ ion with $D_{zfs} = -0.05\ cm^{-1}$, $E/D = 0.33$.

nuclear or uncoupled Mn^{2+} species. This component is present in samples that have been subjected to size exclusion chromatography and so the Mn^{2+} appears to be tightly associated with the enzyme. Reliable quantitation of this signal has not been possible, but comparison of its intensity with that of the excited state spectra for the majority coupled complex indicates that it represents at most a relatively small fraction of uncoupled or half-occupied sites. The signal is unchanged by incubation of the enzyme with 5 mM Mn^{2+} ions. There is no significant difference in the amount of this species between ligand-free and ligand-bound forms.

The spectrum of this mono-Mn^{2+} complex is characteristic of a high spin d^5 metal ion with moderate zero field splitting ($D \leq h\nu$), and simulation of the spectrum (Gaffney & Silverstone, 1993) gives the best estimate of the ground state parameters: $D = -0.05\ cm^{-1}$, $E/D = 1/3$. The Mn^{2+} zero field splitting is much larger than is typical of near octahedral sites in lattices (Kuska & Rogers, 1968) yet smaller than is found for five-coordinated Mn^{2+} [e.g., in Mn superoxide dismutase (Whittaker & Whittaker, 1991)] and most likely represents a low symmetry six-coordinated complex with mixed ligands and distorted geometry.

Spectral Simulations and Estimates of Ground State Parameters: The Pair Hamiltonian. The effective pair Hamiltonian for the binuclear Mn^{2+} complex is given by:

$$H = H_o + H_{exch} + H_{dip} + H_{zfs} + H_{zee} \qquad (15)$$

where the full Hamiltonian H is expanded in perturbations on the molecular electronic Hamiltonian H_o including the Heisenberg exchange term $H_{exch} = J\boldsymbol{S}_1\ \boldsymbol{S}_2$, the magnetic dipolar interaction term $H_{dip} = D_{dip}(3S_{1z}S_{2z} - \mathbf{S_1}\cdot\mathbf{S_2})$ resulting from the mutual interaction of the magnetic dipoles of the two paramagnetic ions, the single-site zero field splitting contribution $H_{zfs} = \Sigma_i D_{zfs}[S_{z,i}'^2 - (1/3)S_i(S_i + 1)] + E(S_{x,i}^2 - S_{y,i}^2)$ that has its origin in spin orbit effects on each metal ion, and the Zeeman interaction $H_{zee} = g\beta\boldsymbol{H}(\boldsymbol{S}_1 + \boldsymbol{S}_2)$ for the paramagnetic ions in an external applied magnetic field.

The pair Hamiltonian for a coupled binuclear high spin Mn^{2+} complex can be constructed by taking the Kronecker product of six-dimensional representation matrices for the independent $S = 5/2$ metal ions (Poole & Farach, 1987). Calculations were performed using the resulting 36-dimensional direct product matrix spanned by the $|M_{s1}\rangle|M_{s2}\rangle$ basis. Explicitly,

$$H = J(\mathbf{S}_{1z} \times \mathbf{S}_{2z} + \mathbf{S}_{1+} \times \mathbf{S}_{2-} + \mathbf{S}_{1-} \times \mathbf{S}_{2+}) + D_{dip}(3\mathbf{S}_{1z} \times \boldsymbol{S}_{2z} - \boldsymbol{S}_{1z}\cdot\mathbf{S}_{2z}) + D_{zfs,1}(\mathbf{S}_{1z}^2 \times \mathbf{1} - (1/3)\mathbf{S}_1^2 \times \mathbf{1}) + E_{zfs,1}/2[(\mathbf{S}_{1+}^2 + \mathbf{S}_{1-}^2) \times \mathbf{1}] + D_{zfs,2}(\mathbf{1} \times \mathbf{S}_{2z}^2 - \mathbf{1} \times (1/3)\mathbf{S}_2^2) + E_{zfs,2}/2[\mathbf{1} \times (\mathbf{S}_{2+}^2 + \mathbf{S}_{2-}^2)] + g\beta H(\mathbf{S}_{1z} \times \mathbf{1} + \mathbf{1} \times \mathbf{S}_{2z}) \qquad (16)$$

where the boldface operators $\mathbf{S}_q$ and $\mathbf{1}$ are six-dimensional representation matrices (spin and unit matrices, respectively), and the symbol $\times$ indicates the Kronecker or outer matrix product. The spin matrices for $S = 5/2$ were taken from Pilbrow (1990) (however, note a number of typographical errors occur in the $\mathbf{S}_+^2$ and $\mathbf{S}_x^2 - \mathbf{S}_y^2$ matrices given in that reference).

Relations Among the Matrix Elements: Irreducible Tensor Operators. The tensor operator formalism (Fano & Racah, 1959; Tinkham, 1964) clearly expresses the relations among the matrix elements of each of the terms in the Hamiltonian (eq 15). Briefly, physical operators (like H_{dip}) are replaced (through application of the Wigner−Eckart theorem) by equivalent operators transforming identically. For example, the products of spin operators ($\mathbf{S}\cdot\mathbf{S}$) appearing in the exchange, dipolar, and zero field splitting terms transform like second order spherical harmonics. This substitution reduces the problem to a small number of unique irreducible components, resulting in a dramatic simplification. Evaluating the 13 unique matrix elements (Table 1) defines all 1296 elements of the Hamiltonian within the pair basis. Although the dipolar and zero field splitting terms superficially have a similar form, their matrix elements are distinct, and their contributions to the spectra are different. For dipolar terms the result is well known (Tinkham, 1964).

$$H_{dip} = -F\sqrt{6}\sum_{\mu'} T_{\mu'}^{(2)} D_{\mu',0}^{(2)}(\phi,\theta,0) \qquad (\mu = 0, \pm1, \pm2) \qquad (17)$$

For the zero field splitting term, similar considerations apply. The zero field operator may be equivalently expressed in irreducible tensor form as

$$H_{zfs,1} = \sum_{\mu'} T_{\mu'}^{(2)}[(\sqrt{6})/3\ D_{zfs} D_{\mu',0}^{(2)} + \mathrm{E}(D_{\mu',2}^{(2)} + D_{\mu',-2}^{(2)})] \qquad (\mu = 0, \pm1, \pm2) \qquad (18)$$

This leads to matrix elements in the coupled representation

$$\langle S'M_s'|H_{zfs}|SM_s\rangle = 2\sum_{\mu'}\langle S'M_s'||H_{zfs,i}||SM_s\rangle A_{M_s,\mu'}\delta_{M_s',M_s+\mu'}[(\sqrt{6})/ 3D_{zfs}D_{\mu',0}^{(2)} + \mathrm{E}(D_{\mu',2}^{(2)} + D_{\mu',-2}^{(2)})]$$

where the $A_{Msm}^{S2S'}$ are the Wigner coefficients and the $\langle S'M_S'||H_{zfs}||SM_S\rangle$ are the reduced matrix elements. The 13 distinct reduced matrix elements for H_{zfs} are different from those calculated for H_{dip} and are listed in Table 1 for reference.

Spin Manifolds and Resonance Fields. The basic structure emerging from the Hamiltonian is described by a ladder of S_T multiplets split by exchange coupling with smaller

intramultiplet splittings determined by the combined dipolar, zero field, and Zeeman interactions. Thus, exchange interactions lift the 36-fold spin state degeneracy of the pair and split the pair states into an exchange ladder with Landé interval rule between states of different total spin $S_T = S_1 + S_2 = |S_1 - S_2|, ..., (S_1 + S_2)$ (Figure 3). Since exchange interactions reflect covalency, these splittings are relatively small for Mn^{2+} ions (typically in the range $|J| = 1-50$ cm^{-1}), the magnitude being determined by geometry and the nature of the bridging ligand(s). A reduction in the metal−ligand interactions by displacement or protonation of a bridging group reduces the covalency pathway for exchange and will be reflected in a decrease in *J*-coupling (Armstrong, 1992).

The ground state magnetic moment of a high spin $S = 5/2$ ion is 5.92β (the largest possible for a transition ion) making dipole−dipole coupling between magnetic moments on neighboring ions a significant perturbation. Dipolar interactions remove M_S degeneracies of the S_T multiplets and mix electronic substates of the exchange ladder with the same M_S value and $\Delta S_T = \pm 2$ (Table 1). The magnitude of the dipolar interaction can be related to structure through the dipole coupling parameter ($D_{dip} = -g^2\beta^2/r^3$) which takes on only negative values and whose exponential dependence on inter-ion separation makes it very sensitive to geometry. The magnitude of D_{dip} extracted from the pair spectra has been regarded as unreliable for distance measurements because of large deviations from the value predicted from point dipole theory for a series of crystallographically defined complexes where the geometry is accurately known (Khangulov et al., 1995). As a result, empirical correlations have been required to extract distance information from the spectra. Much better agreement between experiment and theory has been reported in studies on Mn in MgO and related lattices with the experimentally determined D_{dip} at most about 10% low (Harris, 1972). The relatively large magnitude of D_{zfs} in low symmetry d^5 metal complexes (de Bolster et al., 1973; Birdy et al., 1979) compared to the smaller values that are characteristic of nearly exact octahedral coordination for the oxide lattice may account for the apparent differences. In particular, the significant D_{zfs}, comparable to D_{dip}, observed for the mononuclear Mn site in Mn catalase provides an estimate of D_{zfs} for the metal ions in the binuclear complex indicating that zero field splitting must be taken into account. Since the irreducible tensor elements for H_{dip} and H_{zfs} have opposite signs within the triplet ($S_T = 1$) state (Table 1), the two contributions effectively cancel in the overall splitting (Δ), and neglect of contributions from single site zero field splitting to the intramultiplet fine structure splittings in protein and molecular complexes will thus in general result in an underestimate of D_{dip}. Calculation of both resonance fields *and* polarization (see below) is required to determine both parameters (D_{dip} and D_{zfs}).

Degeneracies left by the combined action of dipolar and zero field perturbations are completely removed in a magnetic field as shown in Figure 11, with EPR transitions being induced when the Zeeman splitting matches the photon energy (the resonance condition, $\Delta E = h\nu$). While the magnetic field defines the quantization axis for the electronic spins, the inter-ion vector is the axis of the dipolar interaction and the Zeeman interaction is anisotropic as illustrated graphically for the triplet state ($S_T = 1$) of the binuclear complex in two orientations, with the applied magnetic field aligned parallel or perpendicular to the pair axis (Figure 11).

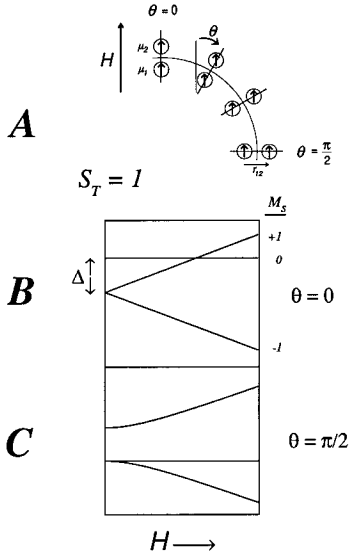

FIGURE 11: Zeeman anisotropy in the presence of dipolar interactions. (A) The orientation of individual magnetic dipoles for the binuclear complex in a strong magnetic field leads to distinct interactions between the two dipoles depending on the relative orientation of the pair axis. (B) Calculated triplet state ($S_T = 1$) splittings with combined Zeeman and dipolar interactions with pair axis parallel to the applied magnetic field direction. (C) Triplet splittings with pair axis oriented perpendicular to the applied magnetic field direction.

With the magnetic field along the pair axis the sublevels split linearly in the field, while in the perpendicular orientation the sublevels split quadratically with increasing magnetic field, leading to broad and complex resonance spectra.

Intensity and Polarization Correlations. EPR transitions are characterized not only by the magnetic field at which resonance occurs but also by intensity and polarization factors relating to the selection rules for magnetic dipole excitation (Hagen, 1982; Hagen et al., 1984; Hendrich & Debrunner, 1988, 1989). For magnetic resonance, polarization is defined by the orientation of the oscillating microwave magnetic field vector relative to the direction of the applied magnetic field. Transitions can then be classified as either π (parallel, $\Delta M_J = 0$), or σ (perpendicular, $\Delta M_J = \pm 1$) according to the selection rules determined by matrix elements of the vector operator components of S (S_x,S_y,S_z). For perpendicular polarization, corresponding to the conventional EPR experiment, the transition probability, P, is given by

$$P_{\pm} = |\sum\sum c^*_j c_i \langle M_{1j}|\langle M_{2j}|S_{1x} + S_{2x}|M_{1i}\rangle|M_{2i}\rangle|^2 = |\sum\sum c^*_j c_i (1/2)\langle M_{1j}|\langle M_{2j}|S_{1+} + S_{1-} + S_{2+} + S_{2-}|M_{1i}\rangle|M_{2i}\rangle|^2 \quad (19)$$

where the c_i and c_j are the coefficients for the *i*th and *j*th components of initial and final state wavefunctions, respectively. In the Zeeman representation (using pure angular momentum basis functions referred to the magnetic field direction), transitions become allowed through the raising and lowering operators S_+ and S_- that connect components in the initial and final states differing by one unit of angular momentum: $\Delta M_J = \pm 1$. For mixed wavefunctions, the transition intensity is computed as the square of the products of (complex) coefficients summed over all basis components.

The selection rule for parallel polarization involves the S_z transition operator, which connects between corresponding

components in the initial and final state wavefunction, leading to a distinct expression for the transition probability:

$$P_o = |\sum\sum c^*_j c_i \langle M_{1j}|\langle M_{2j}|S_{1z} + S_{2z}|M_{1i}\rangle|M_{2i}\rangle|^2 \quad (20)$$

Magnetic resonance induced by S_z requires conjugate angular momentum components to appear in both initial and final states ($\Delta M_J = 0$). This is forbidden for Kramers systems, but can occur for non-Kramers states (even number of electrons, integer spin) through admixture by perturbations that are off-diagonal in the Zeeman representation. Measurement of EPR in parallel polarization requires a resonator that supports a microwave mode having the oscillatory magnetic component in the direction of the applied magnetic field (Hagen, 1982; Hendrich & Debrunner, 1988). The experimentally observed decrease in intensity in parallel polarization to higher magnetic field (Figure 1) is a consequence of the Zeeman interaction unmixing states into pure M_J levels for which the S_z transition is forbidden. EPR polarization experiments can thus be used to measure the composition of electronic wavefunctions in states mixed by perturbations that are not diagonal in the Zeeman interaction.

Accurate simulation of field-swept spectra requires scaling the intrinsic transition probabilities (see above) by the Aasa−Vänngård factor $\gamma_{AV} \sim (d\nu/dH)^{-1}$ to give the correct intensity normalization. The Aasa−Vänngård factor defines the transformation from frequency- to field-domain spectra and can be evaluated using the Hellmann−Feynman theorem, simplifying to a multiplicative factor of $1/g$ (Aasa & Vänngård, 1975). Spectra are calculated by averaging normalized intensities over orientations and convoluting the resulting stick spectra with a Gaussian line shape function:

$$f = (\sigma\sqrt{2\pi})^{-1} \exp[-(H - H_{res})^2/2\sigma^2] \quad (21)$$

where $\sigma = \Gamma_{FWHM}/2\sqrt{(2 \ln 2)}$ is the line width parameter defined in terms of the full width at half-maximum (Γ_{FWHM}) of the Gaussian line. The symmetry of the pair complex allows the averaging grid to be reduced to a longitude

$$I(H) = f\int_0^{\pi} P_q n(T) \gamma_{AV} \sin\theta \, d\theta \quad (22)$$

for calculations in which rhombic terms are neglected. For extremely anisotropic resonances characteristic of dipolar coupled ions with multiplet splitting $\Delta \sim h\nu$, more extensive angular averaging with higher angular resolution is required to obtain smooth spectra.

Ground State Parameters. Pair spectra for the binuclear Mn^{2+} complex reflect the magnitudes of the multiplet splittings in the shifts from $g = 2$, as shown in Figure 12. Evaluation of the complete pair Hamiltonian shows that, in the absence of multiplet splittings ($\Delta = 0$; $D_{dip} = D_{zfs} = 0$), the resonances all coincide (Figure 12, top); for intramultiplet splittings small compared to the microwave energy ($\Delta < h\nu$) (Figure 12, middle), the transitions are centered on $g = 2$ and split by $\Delta H = (h\nu - \Delta)/g\beta$; while for multiplet splittings large compared to the microwave energy ($\Delta > h\nu$) (Figure 12, bottom), transitions are centered at $H = \Delta/g\beta$ and split by $h\nu/g\beta$ contributing frequency-dependent features to the spectra. Transition intensity also varies with S_T state, since the matrix element μ_- or J_- for the transition $M \leftrightarrow M - 1$ has a magnitude proportional to $\chi''_{M,M-1} \sim [S_T(S_T + 1) - M(M - 1)]$ leading to greater intrinsic intensities within

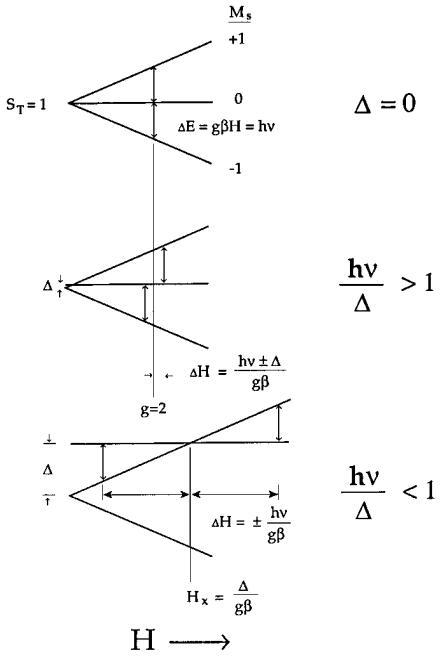

FIGURE 12: Limiting cases for resonance within the triplet state. (Top) Degenerate transitions in absence of dipolar splitting. (Middle) Small spectral shifts associated with small fine structure splittings. (Bottom) Effect of large intramultiplet splittings on the resonance spectrum.

the higher S_T states where the large M_{iS} ($i = 1,2$) components and higher multiplicity occurs. The Q-band spectra (Figure 8) appear to represent the limit of small intramultiplet splittings, with transitions nearly symmetrically disposed about the free electron g value ($g = 2.00$). However, near-cancellation between spin dipolar and zero field contributions to the fine structure splittings in the multiplets will give similar results (see below).

The irreducible tensor elements arising from H_{dip} and H_{zfs} within distinct multiplets of the spin ladder determine the relative magnitudes of the spectroscopic splittings in these states. From Table 1 it is clear that the largest splittings will occur in the lowest paramagnetic state ($S_T = 1$) of the antiferromagnetic spin ladder with progressively smaller splittings in the higher lying states. As a result, population up the spin ladder will give rise to a series of spectral features progressively collapsing around $g = 2$. The multiplicity, intrinsic intensities and the relatively isotropic character of the signals from higher-lying states results in their dominating the spectra, accounting for the basic features of the Q-band spectra (Figure 8). Numerical calculation of X-band spectra in both polarizations (Figure 13) provide estimates of the ground state parameters D_{dip} and D_{zfs} for the fluoride adduct: $D_{dip} = -0.044$ cm^{-1} and $D_{zfs} = -0.05$ cm^{-1}. The magnitude of the dipolar coupling estimated from the calculated spectra is consistent with an inter-ion separation of 3.4 Å, somewhat less than the 3.6 Å separation determined from the low-resolution X-ray crystal structure for the *T. thermophilus* Mn catalase (Vainshtein et al., 1984) but within the range reported for bridged binuclear Mn complexes (Larson & Pecoraro, 1992).

CONCLUSIONS

Multifrequency EPR, microwave polarization studies, and spectroscopic simulations provide an effective approach to extracting ground state parameters for coupled binuclear Mn

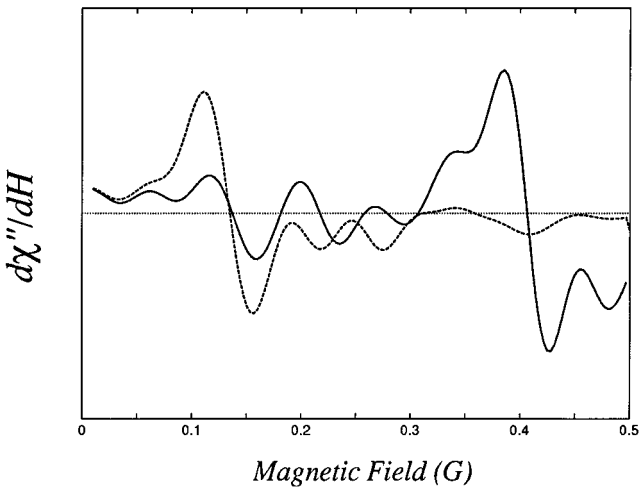

FIGURE 13: Calculated X-band EPR spectra for Mn catalase fluoride complex. Ground state parameters: $J = 10.5$ cm^{-1}; $D_{dip} = -0.044$ cm^{-1}; $D_{zfs} = -0.05$ cm^{-1}; line width, 500 G; microwave frequency, 9.4 GHz; temperature, 10 K. (Solid line) perpendicular polarization; (Broken line) parallel polarization.

complexes including the active site of Mn catalase. The combination of methods allows significantly more information to be extracted from the experimental data, yielding more reliable estimates of the ground state parameters. These parameters reflect key structural elements of the electronic ground state for the coupled binuclear Mn complex, relating to its catalytic reactivity. While further refinement of the parameters is clearly possible, the most important feature is that all the ground state parameters are *small*, characteristic of a complex with only weak electronic interactions between the two metal ions, with values for the exchange interaction (J) typical for oxo/carboxylate bridged Mn complexes (Ménage et al., 1988). A pair of metal ions coupled by only weak electronic interactions appears to be a motif that has evolved in biology for two-electron redox chemistry of dioxygen. This electronic structural motif appears in other contexts in the active sites of oxygen binding metalloproteins hemerythrin (2Fe) (Stenkamp, 1994) and hemocyanin (2Cu) (Katajima & Moro-oka, 1994; Magnus et al., 1994). The leveling of electronic coupling between Mn^{2+} and Mn^{3+} dimers is of special interest in this regard (Ménage et al., 1988). However, weak coupling alone is not sufficient as the basis for reactivity, since the dimanganese interactions in the fluoride-inhibited Mn catalase complex are even weaker than those found for the active reduced enzyme, and other aspects of the active site must be important in determining the chemistry.

Redox chemistry of oxygen species involves *protons* as well as *electrons*. While the Mn ions can participate in *electron* storage during catalysis, other groups must be involved in storing the two protons required for the disproportionation reaction. These groups have yet to be identified in the Mn catalases but based on general principles of biological catalysis are likely to be closely associated with the metal centers. The results of anion binding studies described here suggest that there is a modulation of ligand basicity associated with Mn ligand interactions that may serve in the proton coupling chemistry. This analysis accounts for the most curious feature of the inhibition chemistry, that fluoride [an anion with a high affinity for Mn^{3+} typically stabilizing the higher oxidation state (Bhattacharjee, 1989)] traps Mn catalase in the *reduced* binuclear Mn^{2+} form. Further, this picture accounts for the linkage between anion and proton interactions in the complex implied by the increased affinity for fluoride at low pH. In our view, anion inhibition results when exogenous ligands bind in the active site and displace (or weaken) a bridge in the Mn core (consistent with the observed decrease in J-coupling in the fluoride adduct), increasing its basicity. Lower covalency in the Mn^{2+} complex will tend to increase ligand basicity in the reduced enzyme compared to the oxidized (Mn^{3+} Mn^{3+}) form, favoring protonation of the ligand atom in that form. Proton uptake by the perturbed bridge(s) would stabilize the complex, the active site being *poisoned by protons* entering at the wrong point in the turnover cycle. The bridging ligand may be lost from the complex in this protonated form with insertion of fluoride ions into the bridge position of the dimanganese core, accounting for the dramatic effect of anion binding on turnover chemistry. Modulation of intrinsic ligand basicity by exogenous ligands thus accounts for both the experimentally observed pH dependence of anion affinity and anion effects on exchange coupling. Based on inorganic model studies, protonation of bridging oxygens within a di-(μ -oxo) binuclear Mn complex has recently been proposed as a mechanism for enzymatic peroxide oxidation by Mn catalase (Larson & Pecoraro, 1991).

A similar coupling of anion and proton equilibria has been reported in another peroxide-metabolizing enzyme, cytochrome *c* peroxidase, where there is evidence for addition of fluoride and cyanide as the conjugate acids in forming complexes (Erman, 1974a,b). The conjugate bases of weak acids like hydrofluoric ($pK_a = 3.17$) (Jencks & Regenstein, 1977) undergo hydrolysis in aqueous solution, and it is possible that the neutral molecule (e.g., HF) may have greater access to the Mn catalase active site. Accessibility of the active site by neutral molecules and the exclusion of charged ions could be an adaptation that permits oxygen species (H_2O, H_2O_2, O_2) to move in and out of the active site but restricts access by coordinating anions. However, the observation that highly charged ions like phosphate and borate exhibit similar inhibitory effects on the *T. thermophilus* enzyme make this less likely and favors the alternative picture of proton-coupled equilibria described above.

Figure 14 outlines a proposal accounting for the basic features of anion inhibition of Mn catalase from the combined spectroscopic and chemical studies reported here. The electon and proton requirements of hydrogen peroxide disproportionation are met by the di-μ-oxo-bridged dimanganese core proposed previously on the basis of spectroscopic studies on the oxidized complex (Gamelin et al., 1994). Reduction of the oxidized Mn^{3+} complex leads to the formation of a hydroxide-bridged Mn^{2+} species in which the catalytic protons are associated with the oxygen bridges. Two fluoride ions can bind to Mn in the active site, perturbing the metal complex which becomes protonated, neutralizing the additional charge from F^- and stabilizing the adduct. For the Mn^{2+} enzyme, protonation would convert bridging hydroxides into relatively labile water bridges making them susceptible to exchange reactions leading to insertion of fluoride ions in μ-bridging geometry. Both terminal and μ-bridging geometries are known for halide ligands (Cl^-, F^-) in dinuclear metal complexes (Mathur et al., 1987; Jacobson et al., 1991; Lee & Holm, 1993) supporting the

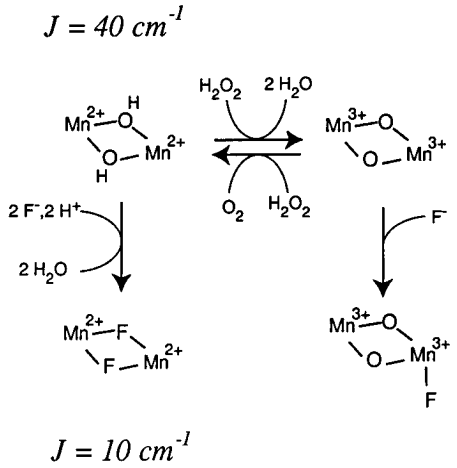

FIGURE 14: Model for anion inhibition of Mn catalase. Fluoride binding to the active site is coupled to protonation of the complex, stabilizing the adduct, and decreasing the magnitude of the exchange coupling, *J*.

proposed bridging role for fluoride ions in $Mn^{2+/2+}$ catalase. The fluoride complex is blocked from further turnover both by the addition of an inhibitory complement of protons and the replacement of the essential oxygen bridges, with weaker electronic interactions between the two high spin Mn^{2+} ions in the inhibited complex being reflected in reduced *J*-coupling.

ACKNOWLEDGMENT

This work represents the results of an undergraduate summer research project performed by A.E.M. in 1994 while visiting as an exchange student from the École Polytechnique Fédérale of Lausanne, Switzerland. The authors would like to thank Christoper Ekberg for assistance in developing the nu_spin program.

REFERENCES

Aasa, R., & Vänngård, T. (1975) *J. Magn. Reson. 19*, 308−315.
Abragam, A., & Bleaney, B. (1970) *Electron Paramagnetic Resonance of Transition Ions*, Oxford University Press, Oxford.
Armstrong, W. H. (1992) *Manganese Redox Enzymes* (Pecoraro, V. L., Ed.) pp 261−286, VCH Publishers, New York.
Berg, J. M., & Holm, R. H. (1982) *Iron Sulfur Proteins* (Spiro, T. G., Ed.) pp 1−66, Wiley, New York.
Beyer, W. F., Jr., & Fridovich, I. (1985) *Biochemistry 24*, 6460−6467.
Beyer, W. F., Jr., & Fridovich, I. (1988) *Basic Life Sci., Oxygen Radicals Biol. Med. 49*, 651−661.
Bhattacharjee, M. N., Chaudhuri, M. K., & Dutta Purayastha, R. N. (1989) *Inorg. Chem. 28*, 3747−3752.
Birdy, R. B., Brun, G., Goodgame, D. M. L., & Goodgame, M. (1979) *J. Chem. Soc. Dalton Trans. 1979*, 149−151.
Boas, J. F., Dunhill, R. H., Pilbrow, J. R., Srivastava, R. C., & Smith, T. D. (1969) *J. Chem. Soc. (A)*, 94−108.
Bowlby, N. & Frasch, W. (1985) *Biochemistry 25*, 1402.
Chenaie, G. M., & Martin, I. F. (1970) *Biochim. Biophys. Acta 197*, 219−239.
Dahlquist, F. W. (1978) *Methods Enzymol. 43*, 270−299.
de Bolster, M. W. G., Nieuwnhuijse, B., & Reedijk, J. (1973) *Z. Naturforsch. 28b*, 104−106.
Erman, J. E. (1974a) *Biochemistry 13*, 34−39.
Erman, J. E. (1974b) *Biochemistry 13*, 39−44.
Fano, U., & Racah, G. (1959) *Irreducible Tensorial Sets*, Academic Press, New York.
Fee, J. A., Sanders, D., Slutter, C. E., Doan, P. E., Aasa, R., Karpefors, M., & Vänngård, T. (1995) *Biochem. Biophys. Res. Commun. 212*, 77−83.
Felton, E. A., Evans, J. B., & Niven, C. F., Jr. (1953) *J. Bacteriol. 65*, 481−482.
Frans, S. D., & Harris, J. M. (1985) *Anal. Chem. 57*, 1718−1721.
Gaffney, B. J., & Silverstone, H. J. (1993) *EMR of Paramagnetic Molecules* (Berliner, L. J., & Reuben, J., Eds.) pp 1−55, Plenum, New York.
Gamelin, D. R., Kirk, M. L., Stemmler, T. L., Pal, S., Armstrong, W. H., Penner-Hahn, J. E., & Solomon, E. I. (1994) *J. Am. Chem. Soc. 116*, 2392−2409.
Hagen, W. (1982) *Biochim. Biophys. Acta 708*, 82−98.
Hagen, W. R., Dunham, W. R., Sands, R. H., Shaw, R. W., & Beinert, H. (1984) *Biochim. Biophys. Acta 765*, 399−402.
Harris, E. A. (1972) *J. Phys. C 5*, 338−352.
Harris, E. A. (1972) *J. Phys. C 5*, 338−352.
Hendrich, M. P., & Debrunner, P. G. (1988) *J. Magn. Reson. 78*, 133−141.
Hendrich, M. P., & Debrunner, P. G. (1989) *Biophys. J. 56*, 489−506.
Henry, E. R., & Hofrichter, J. (1992) *Methods Enzymol. 210*, 129−192.
Hutchings, M. T., Birgeneau, R. J., & Wolf, W. P. (1968) *Phys. Rev. 168*, 1026−1044.
Jacobson, R. R., Tyeklár, Z., Karlin, K. D., & Zubieta, J. (1991) *Inorg. Chem. 30*, 2035−2040.
Jencks, W. P., & Regenstein, J. (1977) *Handbook of Biochemistry and Molecular Biology* (Fasman, G. D, Ed.) Vol. 1, 3rd ed., pp 305−351, CRC Press, Boca Raton, FL.
Katajima, N., & Moro-oka, Y. (1994) *Chem. Rev. 94*, 737−758.
Khangulov, S. V., Barynin, V. V., & Antonyuk-Barynina, S. V. (1990a) *Biochim. Biophys. Acta 1020*, 25−33.
Khangulov, S. V., Barynin, V. V., Voedodskaya, N. V., & Grebenko, A. I. (1990b) *Biochim. Biophys. Acta 1020*, 305−310.
Khangulov, S. V., Goldfeld, M. G., Gerasimenko, V. V., Andreeva, N. E., Barynin, V. V., & Grebenko, A. I. (1990c) *J. Inorg. Biochem. 40*, 279−292.
Khangulov, S. V., Pessiki, P. J., Barynin, V. V., Ash, D. E., & Dismukes, G. C. (1995) *Biochemistry 34*, 2015−2025.
Kliger, D. S., Lewis, J. W., & Randall, C. E. (1990) *Polarized Light in Optics and Spectroscopy*, Academic Press, New York.
Kono, Y., & Fridovich, I. (1983) *J. Biol. Chem. 258*, 6015−6019.
Kuska, H. A., & Rogers, M. T. (1968) *Radical Ions* (Kaiser, E. T., & Kevan, L., Eds.) pp 650−661, Interscience, New York.
Larson, E. J., & Pecoraro, V. L. (1991) *J. Am. Chem. Soc. 113*, 7809−7810.
Larson, E. J., & Pecoraro, V. L. (1992) *Manganese Redox Enzymes* (Pecoraro, V. L., Ed.) pp 1−28, VCH Publishers, New York.
Laskowski, E. J., & Hendrickson, D. N. (1978) *Inorg. Chem. 17*, 457−470.
Lee, S. C., & Holm, R. H. (1993) *Inorg. Chem. 32*, 4745−4753.
Magnus, K. A., Ton-That, H., & Carpenter, J. E. (1994) *Chem. Rev. 94*, 727−736.
Mathur, P., Crowder, M., & Dismukes, G. C. (1987) *J. Am. Chem. Soc. 109*, 5227−5233.
Ménage, S., Girerd, J.-J., & Gleizes, A. (1988) *J. Chem. Soc., Chem. Commun.*, 431−432.
Mouresca, J.-M., Chen, J. L., Noodleman, L., Bashford, D., & Case., D. A. (1994) *J. Am. Chem. Soc. 116*, 11898−11914.
Noodleman, L., & Case, D. A. (1992) *Adv. Inorg. Chem. 38*, 423−470.
Owen, J., & Harris, E. A. (1972) *Electron Paramagnetic Resonance* (Geshwind, S., Ed.) pp 427−492, Plenum, New York.
Palmer, G., Dunham, W. R., Fee, J. A., Sands, R. H., Hzuka, T., & Yonetani, T. (1971) *Biochim. Biophys. Acta 245*, 201−207.
Penner-Hahn, J. E. (1992) *Manganese Redox Enzymes* (Pecoraro, V. L., Ed.) pp 29−45, VCH Publishers, New York.
Pilbrow, J. R. (1990) *Transition Ion Electron Paramagnetic Resonance*, Oxford University Press, Oxford.
Poole, C. P., Jr., & Farach, H. A. (1987) *Theory of Magnetic Resonance*, 2nd ed., Wiley, New York.
Press, W. H., Teukolsky, S. A., Vettering, W. T., & Flannery, B. P. (1992) *Numerical Recipes in C*, 2nd ed., Cambridge University Press, Cambridge.

Radmer, R., & Chenaie, G. M. (1977) *Top. Photosynth. 2*, 303−348.
Reed, C. A., & Orosz, R. D. (1993) *Research Frontiers in Magnetochemistry* (O'Conner, C. J., Ed.) pp 351−393, World Scientific, Singapore.
Rosenweig, A. C., Frederick, C. A., Lippard, S. J., & Nordlund, P. (1993) *Nature 366*, 537−543.
Schonbaum, G. R., & Chance, B. (1976) *The Enzymes* (Boyer, P. D., Ed.) Vol. XIII, pp 363−408, Academic, New York.
Simon, K. P., & Sturm, E. (1992) *Proceedings of the 4th ESO/ST-ECF Data Analysis Workshop*, Garching, May 13−15 (Grosbøl, P. J., & de Ruisjsscher, R. C. E., Eds.) pp 91−97.
Stenkamp, R. E. (1994) *Chem. Rev. 94*, 715−726.
Thinkam, M. (1964) *Group Theory and Quantum Mechanics*, McGraw Hill, San Francisco.
Toftlund, H., Markiewicz, A., & Murray, K. S. (1990) *Acta Chem. Scand. 44*, 443−446.
Vainshtein, B. K., Melik-Adamyan, W. R., Barynin, V. V., & Vagin, A. A. (1984) *Progress in Bioorganic Chemistry and Molecular Biology* (Ovhinnikov, Yu. A., Ed.) pp 117−126, Elsevier, New York.
Vincent, J. B., & Christou, G. (1989) *Adv. Inorg. Chem. 33*, 197−257.
Waldo, G. S., & Penner-Hahn, J. E. (1995) *Biochemistry 34*, 1507−1512.
Waldo, G. S., Fronko, R. M., & Penner-Hahn, J. E. (1991) *Biochemistry 30*, 10486−10490.
Whittenbury, R. (1964) *J. Gen. Microbiol. 35*, 13−26.
Whittaker, J. W. (1994) *Metal Ions in Biological Systems* (Sigel, H., & Sigel, A., Eds.) Vol. 30, pp 315−360 Marcel Dekker, New York.
Whittaker, M. M., & Whittaker, J. W. (1993) *Biophys. J. 64*, 762−772.

BI952126S